forests

Article

Quantifying the Potential Vegetation Distribution under Climate Change: The Case of *Cryptomeria fortunei* in Dongting Lake Watershed, China

Lintong Huang [1,2], Mingke Luo [1], Xia Jiang [1], Peng Zhang [2], Hongxiang Wang [2], Fengtian Hong [2], Ning He [2], Wenxian Guo [2,*] and Yong Niu [1,*]

[1] National Engineering Laboratory for Lake Pollution Control and Ecological Restoration, Institute of Lake Ecology and Environment, Chinese Research Academy of Environmental Sciences, Beijing 100012, China; 201604630@stu.ncwu.edu.cn (L.H.)

[2] School of Water Conservancy, North China University of Water Resources and Electric Power, Zhengzhou 450045, China

* Correspondence: guowenxian@ncwu.edu.cn (W.G.); niu.yong@craes.org.cn (Y.N.); Tel.: +86-15637121238 (W.G.)

Abstract: Potential vegetation distribution is an important study in environmental sciences. We utilized the Mixed Least Squares–Total Least Squares (MLS-TLS) method and the Signal Mode Decomposition method and the Ecological Niche model to identify the inter-correlations of internal climate change factors and constructed an environmental factor response regression model. We identified the resonance periods and trend relationships among climate factors (temperature, precipitation, and evapotranspiration) and found that the evapotranspiration of the watershed interferes with the correlation between temperature and precipitation on a five-year scale. The specific change degree of extreme climate indicators in the region was quantified by the Range of Variability Approach, among which the precipitation indicators were all below 33% (low change). There were significant differences between the key bioclimatic variables and Aspect of the development of suitable vegetation habitats. The difference between the Aspect and average daily air temperature is the main contributor to the spatial distribution of vegetation, and the mutual contribution is 76.19%. Our regression model can effectively simulate the potential distribution of vegetation (r = 0.854). Compared to the MaxEnt model, our regression model can quantitatively and intuitively provide suitable habitat values for *Cryptomeria fortunei* at any given location in the basin. Under future scenarios (2021–2040), suitable habitat for *Cryptomeria fortunei* in the eastern and western regions of the basin is projected to deteriorate further. The research results can provide some help for policymakers to eliminate the potential adverse effects of future climate change on regional ecology.

Keywords: vegetation habitat; mixed least squares–total least squares method; quantitative evaluation; remote sensing; ecological niche model

Citation: Huang, L.; Luo, M.; Jiang, X.; Zhang, P.; Wang, H.; Hong, F.; He, N.; Guo, W.; Niu, Y. Quantifying the Potential Vegetation Distribution under Climate Change: The Case of *Cryptomeria fortunei* in Dongting Lake Watershed, China. *Forests* **2023**, *14*, 614. https://doi.org/10.3390/f14030614

Academic Editor: Nadezhda Tchebakova

Received: 6 February 2023
Revised: 14 March 2023
Accepted: 17 March 2023
Published: 19 March 2023

1. Introduction

In the past century, climate change, as an important manifestation and part of the changing environment, has brought a profound influence on the hydrological cycle process and the Earth's ecosystem [1]. The response relationship between vegetation and climate has always been the focus of global scholars' research reports and attention [2–6]. In addition to being a crucial ecological component, vegetation has a significant impact on human society and is easily impacted by human activity in the global ecosystem. Not only does vegetation contribute to climate change, but it is also one of its positive feedback regulators [7]. However, research shows that human activities are promoting the habitat change of forest vegetation system on large scale and settlement scale from climate level [8].

Climate change has many different spatial and temporal scales, and vegetation responses in different regions are also different. An increase in temperature beyond a threshold enhances vegetation respiration [9]. Changes in precipitation will directly affect forest system productivity [3]; both temperature and precipitation vary over temporal and spatial scales, consequently affecting vegetation distribution. [10,11]. Spatially, the complex distribution of vegetation communities is mainly controlled by altitude. It has also been reported that when AT and precipitation become factors limiting plant growth, they may have a greater impact on local vegetation than altitude [12]. If we can clarify the response relationship between vegetation distribution and AT, precipitation, and regional topography, it will provide intuitive guidance for the current vegetation suitability and future regional ecological restoration. However, at present, most of the research uses the normalized difference vegetation index (NDVI) to represent vegetation for climate change research [6,13]. However, NDVI is based on band interpretation and has low sensitivity to areas with high vegetation density, so it cannot fully reflect the distribution and growth status of vegetation in the area [14]. Furthermore, the complex meteorological and hydrological systems contain various interactions between meteorological elements. Under the influence of climate change and human activities, individual meteorological time series and their interactions tend to become more complex, and simple correlation tests between two variables may not be able to demonstrate their intrinsic correlations and their evolution [15]. Over a given time period, the variations in hydro-meteorological sequences do not exhibit fixed periodic motions but rather contain changes and local fluctuations across multiple time scales. The process characteristics of these nonlinear and non-stationary states can be identified through the Signal Mode Decomposition method [16]. Therefore, clarifying the relationship between the internal factors of climate change on temporal and spatial scales, as well as quantifying the response process of climate and vegetation spatial distribution, remains a work of practical importance.

The Ecological Niche model based on existing species distribution data and ecologically meaningful meteorological data has been widely used by ecologists to analyze and predict the potential distribution of species in time and space [17–20]. Its results can be used as a species habitat suitability index for qualitative analysis in space [21]. The MaxEnt model, which models species distribution prediction using a maximum entropy algorithm based on basic data, has been applied to Point Reyes Bird Observatory (http://www.prbo.org, accessed on 15 January 2022) and Atlas of Living Australia (http://www.ala.org.au, accessed on 15 January 2022) [17,22]. Therefore, it is a new idea to seek and quantify species' responses to climate through the Ecological Niche model.

People can use the MaxEnt model to understand the contribution of different factors to species distribution but cannot intuitively obtain the response relationship between different factors and species distribution [21]. The least squares method is a commonly used method to solve curve fitting problems, which seeks to minimize the sum of squared errors to determine the best matching function corresponding to the data, thereby intuitively expressing the relationship between the independent and dependent variables and reflecting their physical meanings. The Mixed Least Squares–Total Least Squares (MLS-TLS) method is an advanced least squares method structure [23]. It is a method that can eliminate noise from the covariance matrix, subtracting the noise influence term first, then inverting and solving the matrix to obtain the least squares solution. Therefore, based on the reliable results of the MaxEnt model, constructing a multi-factor relationship model through the MLS-TLS method is highly meaningful work.

Dongting Lake (DTL) wetland is one of the 200 important ecological regions in the world, and it is very representative to choose the DTL basin as the study area [24]. Affected by both natural factors and human activities, DTL wetland plants show zonal distribution characteristics [25]. Paying attention to the habitat development of wetland plants in the DTL basin is of great significance to the maintenance of global wetlands ecosystem functions. Zhang et al. found that climate change has threatened DTL wetland vegetation by 59.19% from 2000 to 2019 [5]. Therefore, taking the DTL basin as the research object has high ecological value and reference significance for species diversity protection in other important ecological regions in the world under the background of climate change.

In our study, our goal is to quantify the relationship between climate and vegetation habitat (spatial distribution). However, we also focused on and clarified the relationship and trend within the climate (AT, precipitation, and evapotranspiration) and quantified the change degree of extreme regional climate. More specifically, the following questions are addressed: (1) Are there interfering scenarios of correlations between regional climates? (2) What are the contribution rates of different climatic factors to suitable vegetation habitats on a spatial scale? (3) An intuitive and reliable model of Climate–Vegetation Suitable Habitat Response Regression (CSHRR) is proposed. We employed the Signal Mode Decomposition method to identify the climate change trend and utilized the Cross Wavelet Transform and Local Running Correlation Coefficient to elucidate the correlation between climate factors. Moreover, the Range of Variability Approach was employed to quantify the extent of extreme climate change within the basin. Subsequently, we constructed a regression model by coupling the MaxEnt model with the MLS-TLS method.

2. Materials and Methods

2.1. Study Area

The DTL Basin (24°63′–30°29′ N, 107°25′–114°24′ E) is an important sub-basin in the middle reaches of the Yangtze River Basin, which flows through six provinces and one municipality directly under the Central Government of China (Figure 1). Many water systems in the basin flow into the Yangtze River through Chenglingji Hydrological Station in Hunan Province. The basin area is 26.28 × 10^4 km^2, accounting for 14.6% of the Yangtze River basin area [17]. The DTL basin belongs to a typical subtropical monsoon humid climate, with four distinct seasons and simultaneous rain and heat. The average annual precipitation is 1200 mm to 1500 mm, and the average annual temperature is 17 °C, with the lowest temperature in January and the highest temperature in July. The vegetation types in the basin are mainly evergreen coniferous forest, evergreen broad-leaved forest, and *Salix* woody plants [25].

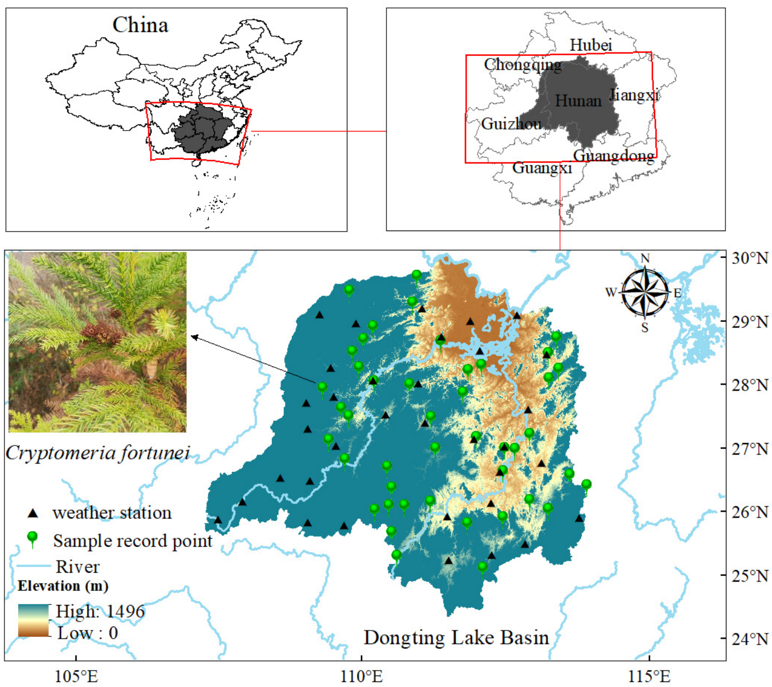

Figure 1. Location of the Dongting Lake watershed and distribution points of *Cryptomeria fortunei*.

Cryptomeria fortunei Hooibrenk ex Otto et Dietr (*Cryptomeria fortunei*), belongs to the family Cupressaceae and is a species of evergreen coniferous tree endemic to China [26]. It can grow up to 48 m tall with a diameter of over 2 m at breast height and has a narrow conical or conical-shaped crown. It prefers a warm and humid mountainous climate with cool summers and well-drained sandy soil while avoiding water-logged areas. The bark is reddish-brown and fibrous, peeling off in long strips. The larger branches are nearly whorled, spreading, or drooping, while the smaller branches are slender and often drooping. The leaves are awl-shaped, slightly inwardly curved, with a length of 1–1.5 cm and stomatal lines on all four sides. The leaves on fruiting branches are usually shorter than those on young trees or sprouting branches, which can reach up to 2.4 cm in length with stomatal lines on all sides [27]. It is commonly found growing in wet mountainous forests or open areas at an altitude of 500 to 1300 m in the DTL basin, where it is considered a wild forest species. *Cryptomeria fortunei*, as one of the evergreen coniferous forests widely distributed in the DTL watershed, is sensitive to climate change and is a favored research object in dendrohydrology and dendroclimatology [28]. Its growth distribution is an important proxy data for reconstructing the evolution law of hydrology and climate in the historical period. Therefore, *Cryptomeria fortunei* was selected as the indicator species in this study.

2.2. Data preparation

2.2.1. Data Source

Meteorological data were daily data sets of 34 weather stations in the DTL basin from 1961 to 2019. Mean air pressure, sunshine hours, relative humidity, wind speed, and maximum, minimum, and average air temperature were used to calculate potential evapotranspiration (ETo). The China Meteorological Data Service Center (http://data.cma.cn/ accessed on 1 March 2021) provided these meteorological data. Raster data includes bioclimatic variables and elevation. Bioclimatic variables are 19 variables with biological significance obtained from monthly temperature and precipitation values, and elevation data is processed to obtain slope and Aspect data. All raster data resolution is 30 s and is provided by WorldClim (https://www.worldclim.org/, accessed on 1 September 2022). In this study, all raster data are georeferenced and corrected. The current bioclimatic variable time series runs from 1970 to 2000, while the future bioclimatic variable time series runs from 2021 to 2040. Regarding future climate scenarios, most studies are based on the Coupled Model Intercomparison Project Phase 5 (CMIP5), while the new version, CMIP6, shows significantly higher climate sensitivity [29]. CMIP6 models simulate the climate system closer to observational results, with less uncertainty, and allow for a wider exploration of future outcomes. SSP245 is an updated RCP4.5 scenario, where radiative forcing will stabilize at 4.5 W/m^2 in 2100, and is a commonly used scenario for assessing species distribution under future scenarios [30]. According to the research results [31], the following six variables (Table 1) are determined to be bioclimatic variables required for the study after spatial data autocorrelation is removed. The longitude and latitude data of indicator species are from National Specimen Information Infrastructure (http://www.nsii.org.cn/2017/home.php, accessed on 1 September 2022) and the Chinese Virtual Herbarium (https://www.cvh.ac.cn/, accessed on 1 September 2022).

Table 1. Bioclimatic variables and their abbreviations.

Bioclimatic Variables	Abbreviation	Bioclimatic Variables	Abbreviation
Mean diurnal air temperature range	MDA	Mean temperature of coldest quarter	MTC
Isothermality	–	Annual precipitation	AP
Max temperature of warmest month	MTW	Precipitation of the warmest quarter	PWQ

Note: These data are from WorldClim (https://www.worldclim.org/, accessed on 1 September 2022).

2.2.2. Species Occurrence Data

In this study, a total of 104 records of occurrence data for *Cryptomeria fortunei* were collected. Furthermore, to avoid the adverse effects of spatial autocorrelation and pseudo-replication of occurrence data on the model's results, we set the buffer range to 10 km to select distribution points of the *Cryptomeria fortunei*. Finally, 70 species occurrence records were retained for modeling after removing highly spatially autocorrelated and duplicate records.

2.3. Methods

2.3.1. Time-Varying Characteristics of Meteorological Elements and Signal Mode Decomposition Method

For the meteorological series, we employed the non-parametric Mann–Kendall Test and Pettitt's Test [32] to identify the abrupt changes in the basin climate variables (temperature, precipitation, ETo) and then used Signal Mode Decomposition Method to identify their characteristics within the basin. Abrupt changes and the corresponding year indicate a turning point in the trend of the meteorological factor at that watershed, which is generally considered to be the accumulation of disturbance effects to the point of extreme value. Complete Ensemble Empirical Mode Decomposition with Adaptive Noise (CEEMDAN) has broad application prospects in signal prediction and decomposition [33,34]. It can deal with data sequences with complex changes and non-stationary and multi-time scale characteristics. By decomposition, accurate and complete components with different fluctuation periods are obtained locally [28]. The *i*-th intrinsic mode component obtained by CEEMDAN decomposition is $\overline{C_i(t)}$, and its specific core algorithm is as follows:

(1) The new signal was decomposed by Empirical Mode Decomposition (EMD) to obtain the first-order intrinsic mode component C_1 [35].

$$E(\mu) = C_1^j(t) + r^j \quad (1)$$

In the formula $\mu = x(t) + (-1)^k \omega v^j(t)$, v^j is a Gaussian white noise signal satisfying the standard normal distribution, j was the number of white noise added, ω was the standard table of white noise, $x(t)$ was the original signal, k was the signal-to-noise ratio, and r was the residual after decomposition.

(2) The first residual $r_1(t)$ was obtained by subtracting the first intrinsic mode component $\overline{C_1(t)}$ (the first intrinsic mode component was obtained by the overall average of the j mode components) from the original signal $x(t)$.

(3) Add the positive and negative paired Gaussian white noise in $r_1(t)$ to obtain the new signal, and use EMD to decompose the new signal to obtain the first mode component F_1. Repeat step 2 until the residual signal is a monotonic function. At this time, the number of intrinsic mode components is N, and the original signal is expressed as follows:

$$x(t) = \sum_{N=1}^{N} \overline{C_N(t)} + r_N(t) \quad (2)$$

(4) The final intrinsic mode function (IMF) value was determined by calculating the total average value across the period of each intrinsic mode function. The noise level decreases as the IMF component sort increases [36]·

2.3.2. De-Interference Meteorological Analysis Technology

For two time series, if a single fixed value is used to express the correlation between them, the intermediate change process is ignored, which may lead to misjudgment of their correlation [37]. We combined the Cross Wavelet Transform (XWT) method and the definition of Partial Correlation and proposed De-interference Meteorological Analysis Technology to clarify the relationship between climate variables (AT, precipitation, ETo). The XWT seeks the correlation between the time domain and frequency domain by analyzing the common spectral signals between sequences x_n, y_n [38]. This technology first uses XWT to diagnose the common period and periodic trend relationship among AT, Precipitation, and ETo. The XWT of two time series, x_n and y_n, can be defined as ${M_n}^X(l)$, ${M_n}^Y(l)$. The Cross Wavelet Spectrum Formula is as follows:

$$ {M_n}^{XY}(l) = {M_n}^X(l){M_n}^{Y^*}(l) \tag{3} $$

where ${M_n}^{Y^*}(l)$ is the complex conjugate of ${M_n}^Y(l)$, and ${M_n}^{XY}(l)$ was the crossed wavelet spectrum. The continuous cross-wavelet power spectrum is tested by calculating the red noise spectrum ${R_K}^X$ and ${P_K}^Y$ of x_n and y_n. The theoretical distribution of cross wavelet power of two time series can be found in references [39]; the formula is as follows:

$$ D\left(\frac{\left|{M_n}^X(t){M_n}^{Y*}(t)\right|}{\sigma_X\sigma_Y}\right) = \frac{Z_\nu(p)}{\nu}\sqrt{{R_K}^X{P_K}^Y} \tag{4} $$

where $Z_\nu(p)$ represents the confidence degree associated with the probability p, and the probability distribution function is defined by the square root of the product of two χ^2 distributions; σ_X and σ_Y are the standard deviations of x_n and y_n, respectively.

After using the XWT to identify whether there is interference and its period between the meteorology in the watershed, the partial correlation [40] was used to determine the relationship between the elements. Local Running Correlation Coefficient (LRCC) represents the changing trend of the correlation between two factors under a fixed time window [41]. LRCC was widely used, and its principle and calculation process can be found in the references [42]. According to partial correlation theory and LRCC window characteristics, the analytical expression of the meteorological correlation process after removing interference factors is as follows:

$$ \lambda(t_i) = \frac{r_{\alpha,\beta}(t_i) - r_{\alpha,\gamma}(t_i) \times r_{\beta,\gamma}(t_i)}{\sqrt{(1 - r_{\alpha,\beta}(t_i)^2) \times (1 - r_{\beta,\gamma}(t_i)^2)}} \tag{5} $$

where $r_{\alpha,\beta}(t_i)$, $r_{\alpha,\gamma}(t_i)$ and $r_{\beta,\gamma}(t_i)$ are the LRCC between the two meteorological elements, respectively, and i is the serial number.

2.3.3. Extreme Climate Range of Variability Approach

In this study, RClimDex software was used to control the quality of daily data of AT and precipitation from 1961 to 2019 as input data. Through statistical analysis of various extreme climate indicators, nine extreme temperature and precipitation indicators were obtained (Table 2). Combined with the Range of Variability Approach (RVA) [43], the change degree of extreme temperature and precipitation in the basin was explored, and the calculation Formula of the change degree is as follows:

$$ V_i = \left|\frac{Y_\xi - Y_\tau}{Y_\tau}\right| \times 100\% \tag{6} $$

$$ V_\tau = \eta \times Y_T \tag{7} $$

where V_i is the change degree of the i-th meteorological index; Y_ξ and Y_τ are the actual number of years and the expected number of years that fall within the RVA target threshold after the meteorological index changes; η is the proportion of the index falling within the RVA target threshold before being disturbed; Y_T is the total number of years after the change of meteorological indicators.

Table 2. Extreme temperature and precipitation indicators.

Air Temperature Index	Abbreviation	Precipitation Index	Abbreviation
Warm Days	TX90p	Simple Daily Intensity Index	SDII
Warm Nights	TN90p	Max one-day Precipitation Amount	RX1D
Ice Days	ID	Extremely Wet Days	R99p
Frost Days	FD	Very Wet Days	R95p
Summer Days	SU	Number of Very Heavy Precipitation Days	R20
Warm Spell Duration Indicator	WSDI	Number of Heavy precipitation Days	R10
Cold Spell Duration Indicator	CSDI	Max five-day Precipitation Amount	RX5day
Growing Season Length	GSL	Consecutive Wet Days	CWD
Diurnal Temperature Range	DTR	Consecutive Dry Days	CDD

2.3.4. MaxEnt Model and Geographical Detector

The MaxEnt model is a Niche model based on the maximum entropy theory and calculated through species distribution information and living conditions [19]. The model has a self-inspection function, which can automatically generate Receiver Operating Characteristic (ROC) curves to evaluate the results [20]. The area under curve (AUC) of ROC is not affected by the judgment threshold, so it is recognized as the best evaluation index of model prediction accuracy at present [17]. The value range of AUC is 0 to 1. The larger the value is, the farther the AUC is from the random distribution and the more accurate the prediction effect will be.

We imported the collected geographic distribution data of *Cryptomeria fortunei*, 19 climatic variables, and 3 terrain factors (DEM, slope, and Aspect) into the MaxEnt model and ran it once while removing variables with zero contribution. For any two highly correlated environmental variables (r > 0.8), the variable with the greater contribution to the response was retained [44]. Among the initial 22 variables, we ultimately selected 7 environmental variables for modeling, and after 10 runs, we obtained the distribution of *Cryptomeria fortunei*. The AUC derived in this study was 0.832, indicating that the species distribution results obtained by the model were credible (Figure 2). Jackknife results showed that MDA had the highest contribution to the model, followed by Aspect, MTC, Isothermality, PWQ, MTW, and AP. The overall gain of these variables reached 0.47. The Jackknife test reflects the importance of explanatory variables based on permutations, and these results indicate that each variable contributes to the gain of the model. Therefore, all included explanatory variables contribute to improving the predictive probability, resulting in higher reliability [45].

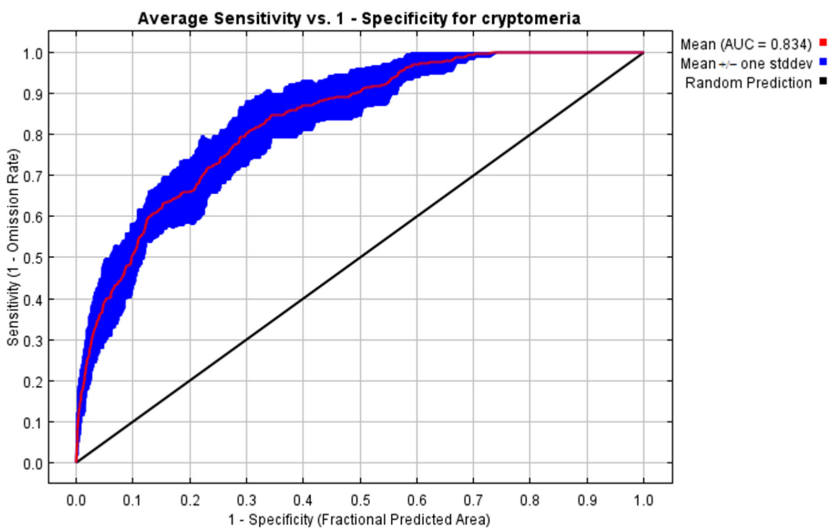

Figure 2. Receiver Operating Characteristic (ROC) curve for habitat suitability prediction of *Cryptomeria fortunei*.

GeoDetector, i.e., Geographical Detector, is a set of statistical methods to quantitatively reveal the driving force of spatial differentiation of each element [46]. The basic idea is that if the spatial distribution of the independent variable is similar to that of the dependent variable, then the independent variable has an important influence on the dependent variable. The greater the similarity, the greater the degree of influence [47]. GeoDetector helps us quantitatively analyze the driving forces affecting the suitable habitats of watershed plants from the perspective of spatial heterogeneity. The Geographical Detector consists of four modules: Interaction detector, Ecological detector, Factor detector, and Risk detector. For specific modules and methods, please refer to the references [48]. Geographical Detector requires that the data type of the independent variable input is discrete. Therefore, we refer to Chen et al. and use the natural breakpoint method to divide all independent variables into seven levels [49].

2.3.5. Mixed Least Squares–Total Least Squares (MLS-TLS)

Least-squares (LS) based algorithms are often used in economic demonstration, machine learning, and remote sensing inversion [50]. The mixed least squares method is based on the difference of the coefficient matrix; for the coefficient matrix A and the matrix X to be obtained, the method of solving the parameters by the coupled least squares method and the total least squares method [51]. In this study, raster data were imported into Stata software for programming (StataCorp LP, College Station, TX, USA). The basic mathematical principles are as follows:

$$A_1X_1 + (A_2 + E_{A_2})X_2 = L + E_L \tag{8}$$

$$R = Q^TP = Q^T[A_1\ A_2\ L] = \begin{bmatrix} R_{11} & R_{12} & R_{1L} \\ 0 & R_{22} & R_{2L} \end{bmatrix} \tag{9}$$

where R is the matrix of $m \times (n+1)$; Q is the m-order orthogonal matrix; A is the coefficient matrix, and $A = [A_1 \quad A_2]$, $A_1 \in R^{m\times n_1}$, $A_2 \in R^{m\times n_2}$, $X_1 \in R^{n_1}$, $X_2 \in R^{n_2}$; L is the observation vector; p is an augmented matrix; $R_{11} \in R^{n_1\times n_1}$ is an upper triangular matrix, $R_{12} \in R^{n_1\times n_2}$, $R_{1L} \in R^{n_1\times 1}$, $R_{22} \in R^{(m-n_1)\times n_2}$, $R_{2L} \in R^{(m-n_1)\times 1}$ [46].

$$R_{11}X_1 + R_{12}X_2 = R_{1L} \tag{10}$$

$$R_{22}X_2 = R_{2L} \tag{11}$$

$$X = [X_1^T \quad X_2^T]^T \tag{12}$$

The TLS method is used to solve Equation (11) to obtain X^2, and after putting X^2 into Equation (10), the LS method is used to solve X_1, then X is obtained.

2.3.6. The Climate–Vegetation Suitable Habitat Response Regression Model (CSHRR Model)

Based on the results of the MaxEnt model, the Climate–Vegetation Suitable Habitat Response Regression (CSHRR) model was constructed using MLS-TLS. The habitat in the model is presented as a continuous change value of 0 to 1 in the raster layer. The closer the value is to 1, the better the habitat suitability is, and the more suitable the species is in the area. We divided the watershed habitat quality values into five classes, including excellent (0.7–1), good (0.45–0.7), average (0.25–0.45), poor (0.1–0.25), and unsuitable habitats (0–0.1). The Formula of the CSHRR model is as follows:

$$H_0 = \beta_0 + \beta_1 Variable_j + \beta_{2ij} Controls_{ij} + \beta_k T_j + \varepsilon_0 \tag{13}$$

where H_0 is the habitat value of the target species; β_1 and $Variable_j$ are the correlation coefficients of explanatory variables and their values in raster J, respectively. β_{2ij} and $Controls_{ij}$ are the correlation coefficient of control variable i and its value at raster J, respectively. T_j and β_k are the level value of the measure index at raster J and the correlation coefficient corresponding to the level. ε_0 is the error term; β_0 is a constant term. The value of $Controls_{ij}$ is the natural log plus 1, and the value range of H_0 is 0 to 1.

3. Results

3.1. Temporal Characteristics and Mode Trends of Climate

The Mann–Kendall Test showed that the AT (maximum, average, and minimum) all passed the 99% significance test, and their statistics were 3.27, 4.58, and 5.93, respectively. Precipitation and ETo did not pass the significance test, and their statistics were 0.54 and −0.51, respectively. Figure 3 displays the interannual value of each climate component. We use Pettitt Test to identify the actual abrupt change years of each factor, and the abrupt change points of different factors are different. The minimum temperature and average temperature change year are both in 1997, while the maximum temperature abrupt change time lags behind by one year. Therefore, we believe that the actual abrupt change year of temperature in the study area can be set as 1997. In addition, the interannual fluctuation of the average temperature maintains a strong synchronization with the maximum and minimum temperatures, so the average temperature is used in the subsequent analysis.

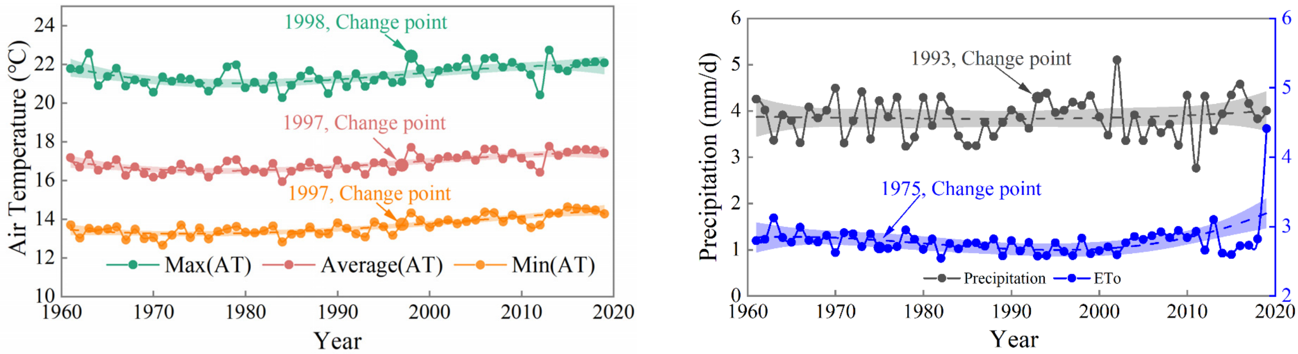

(**a**) Maximum, average, and minimum air temperature

(**b**) Precipitation and evapotranspiration

Figure 3. Interannual variation of meteorological elements.

CEEMDAN was used to analyze AT, precipitation, and ETo and the results are shown in Figure 4. Rainfall has 5 IMF components, while AT and ETo have 4 IMF components. The IMF component of each element better reflects the fluctuation and change characteristics of the original sequence in different periods. The change frequency and amplitude of the IMF1 component of rainfall are faster and higher than those of the other two types of elements, while the ETo lags behind the AT. The IMF5 component of precipitation shows a decline cycle (1974–1986) before the abrupt change (1993). By analyzing the trend, we can see that the AT and ETo show an upward trend as a whole, while the precipitation shows a fluctuating state. Rainfall increased from 1985 and reached its maximum in 2010, while ETo basically fell back to the state in 1990 and continued to rise after that.

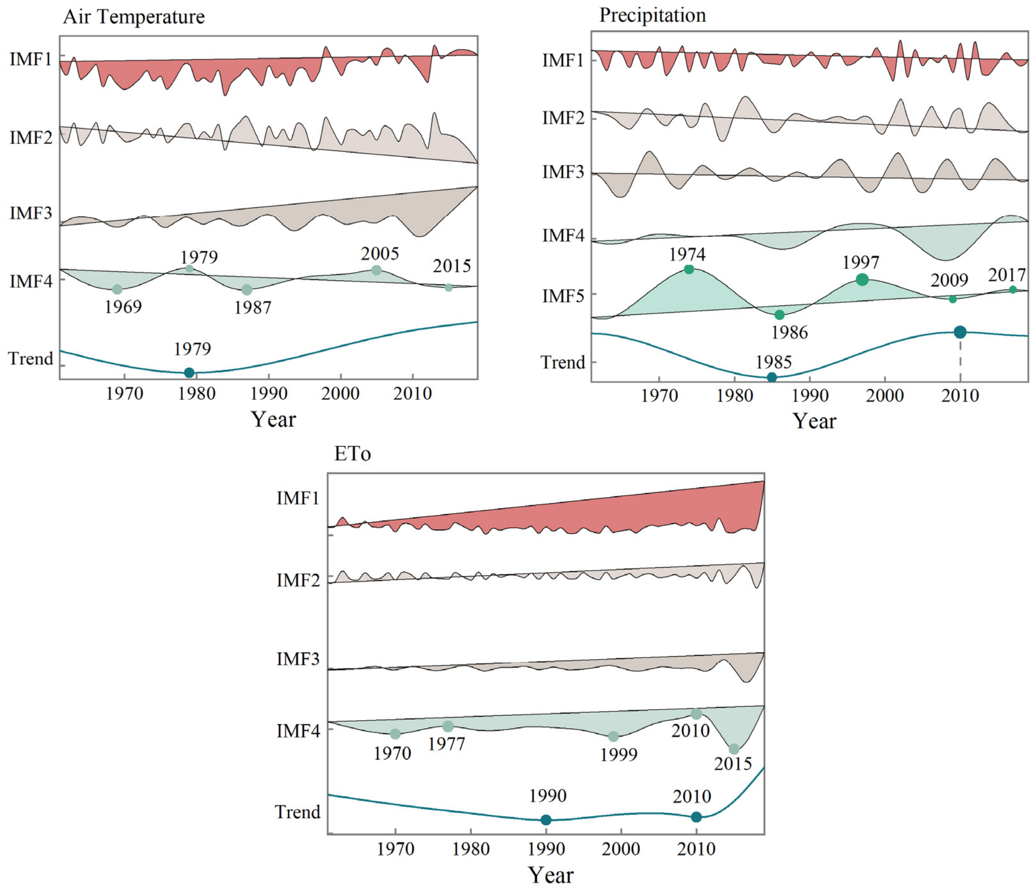

Figure 4. Mode decomposition of meteorological elements.

3.2. Climate Periods and Their Correlation Analysis

The analysis results of XWT and Wavelet Coherence (WTC) are shown in Figure 5. In the high-energy region (XWT), both AT, precipitation, and ETo pass the red noise test with a confidence level of 95%. There is a negative correlation between AT and precipitation on a three-year scale and a positive correlation between AT and ETo on a four-year scale. AT was 1/4 period later than precipitation, while ETo was 1/4 period ahead. The result was similar to the trend of the IMF component. In the low-energy region (wavelet coherence), AT-precipitation and AT-ETo still maintained opposite characteristics in terms of phase and period but showed multi-time-scale positive correlations with ETo. The phase correlation between precipitation-ETo is negative, but the change of the phase relationship between the two on the five-year scale shows uncertainty, which means that the response of AT-precipitation may be mixed with the interference of ETo.

After filtering the influence of ETo on rainfall (Figure 6), the annual correlation curve between AT-precipitation removes the negative correlation characteristics. The correlation results were centered around 0.7, indicating a positive correlation. This is consistent with the arrow pointing to the right trend of AT precipitation on the five-year time scale in the WTC, suggesting that the LRCC in this study is reasonable. It is worth noting that before the abrupt change (1962–1967), there was a high negative correlation between AT-precipitation.

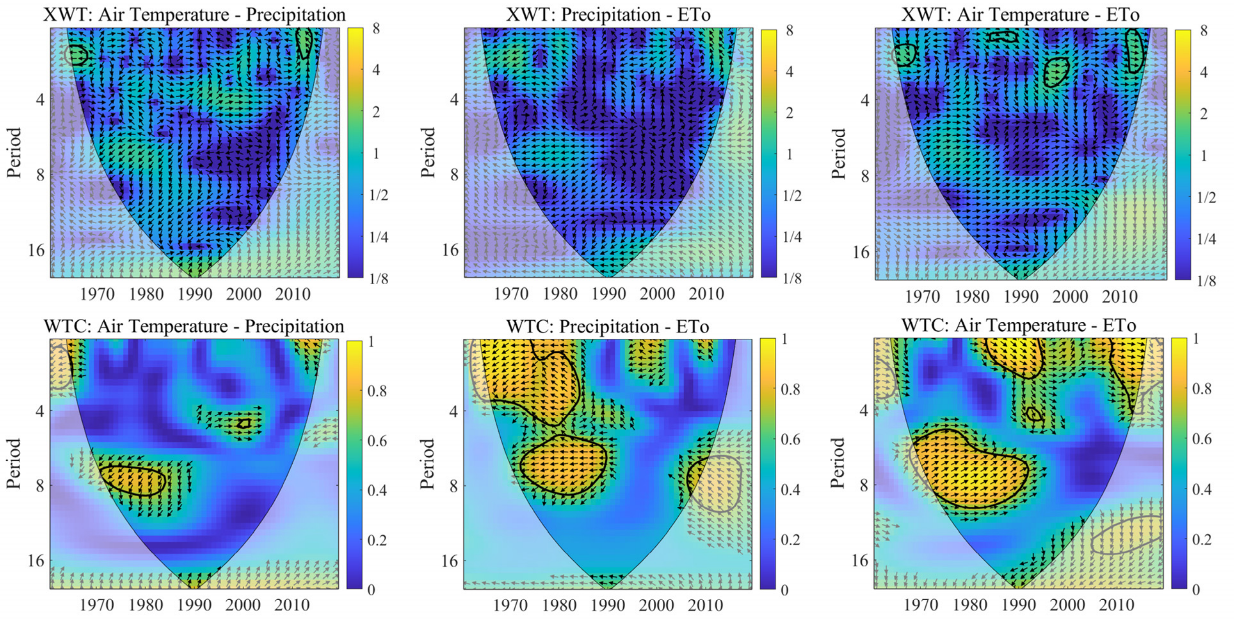

(a) The relationship between temperature and precipitation (b) The relationship between precipitation and ETo (c) The relationship between temperature and ETo

Figure 5. Cross Wavelet Transform of AT, precipitation, and ETo. **Note:** The region surrounded by the influence cone is the effective spectrum value, the remaining regions represent the invalid spectrum value, and the region surrounded by the thick line indicates that it has passed the test of the red noise standard spectrum at the 0.05 significant level. The arrow shows the phase relationship between the two, the right (left) arrow denotes a positive (negative) correlation, the up (down) arrow denotes a phase difference of 90°, and the timing is advanced (delayed) by 1/4 period.

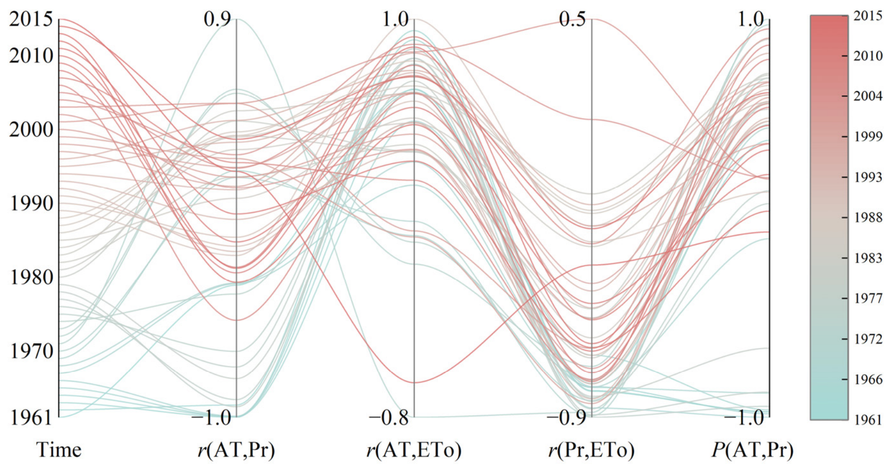

Figure 6. Dynamic correlation between AT and precipitation. **Note:** According to WTC, the LRCC of this study is 5 years. r(AT,Pr) is the LRCC of AT-precipitation, r(AT,ETo) is the LRCC of AT-ETo, r(Pr,ETo) is the LRCC of precipitation-ETo, P(AT,ETo) is the actual correlation coefficient of AT-precipitation.

3.3. Assessment of Watershed Climatic Environment

AT and precipitation are the most direct factors reflecting climate change [52]. Further quantitative analysis of their change degree will help us to judge the habitat status of vegetation in the basin. The RVA method is used to evaluate the extreme indicators of AT and precipitation, and the results are shown in Figure 7. For AT indicators, Warm nights (TN90p) and Warm days (TX90p) have changed moderately (between 33% and 66%), which is in line with the current global warming trend. The rainfall indicators were all maintained below 33% (low change), with the lowest change in Consecutive Dry Days (CDD) and Extremely Wet Days (R99P) and the greatest change in R10 (19%). Changes in extreme temperature and rainfall indicators can quantitatively support the conclusion that the current watershed climate environment is stressing the survival of native vegetation [5].

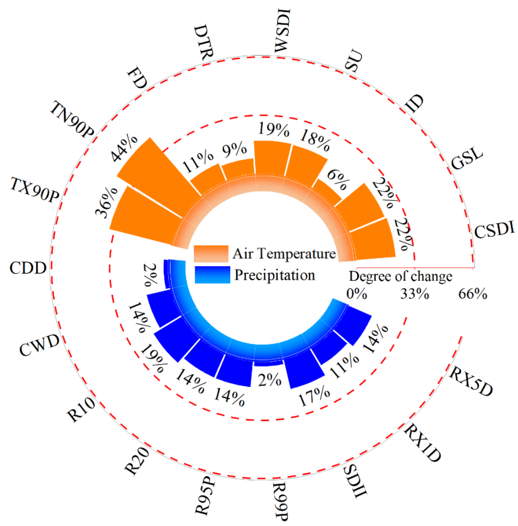

Figure 7. Extreme precipitation and temperature change degree.

3.4. Analysis of the Factors Influencing Species-Appropriate Habitat

We input the MaxEnt model to simulate the spatial distribution of the representative vegetation *Cryptomeria* in the research area based on current bioclimatic variables derived from AT and precipitation (1970–2000). It was found that the contribution rates of Aspect, MDA, AP, MTW, Isothermality, MTC, and PWQ to the indicator species were 46.3%, 25.5%, 12.9%, 7.1%, 4.8%, 2.9%, respectively.

Further understanding the driving forces of vegetation habitat suitability from spatial heterogeneity is a prerequisite for constructing the CSHRR model. The quantitative contribution of 7 factors to vegetation habitat in space is shown in Figure 8. The Geographical Detector shows that Aspect and MDA still maintain a high contribution rate in space, which is 43% and 39%, respectively. However, the spatial promotion effect of MTC on vegetation habitat exceeded AP at this time, reaching 26%. On the basis of the above research, the influence of driving forces on the suitable habitat for vegetation has been analyzed from both external and internal aspects. The external analysis results are shown in Figure 9, and the factor interactions show nonlinear superposition. In particular, the interaction group of Isothermality with AP, MTW, PWQ, and the interaction group of AP with MTW; Aspect are a nonlinear enhancement, and the other interaction groups are bi-nonlinear enhancements, which indicates that the joint action of these factors is beneficial to promote the development of suitable vegetation habitats. The internal analysis results are shown in Figure 10. We found that MDA, Aspect, MTW, MTC, and Isothermality have relatively high contribution rates at 1–4 levels, while PWQ and AP are concentrated at 6–7 levels, and the driving forces at the same level show a trend of ebb and flow.

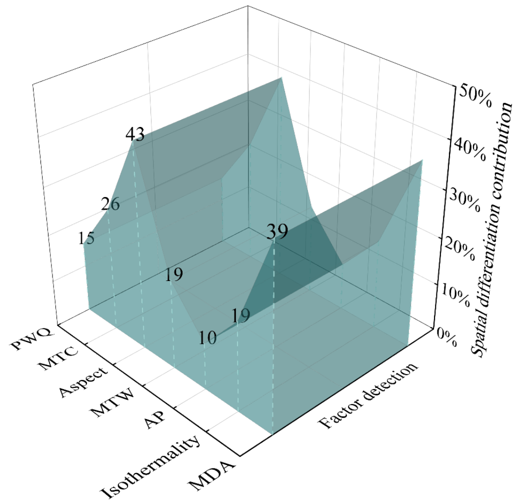

Figure 8. Contribution of Driving Forces to Spatial Heterogeneity.

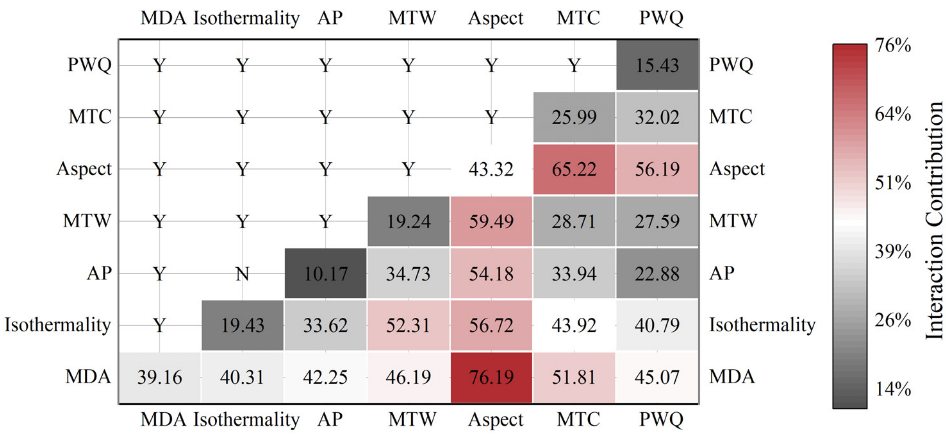

Figure 9. Thermodynamic diagram of driving force interaction. **Note:** nonlinear enhance: (q(x1∩x2) > q(x1) + q(x2); bi-nonlinear enhance: q(x1∩x2) > Max(q(x1), q(x2)). Y indicates that there is a significant difference between the two factors on the vegetation habitat at the 95% confidence level, and **N** indicates that it is not significant.

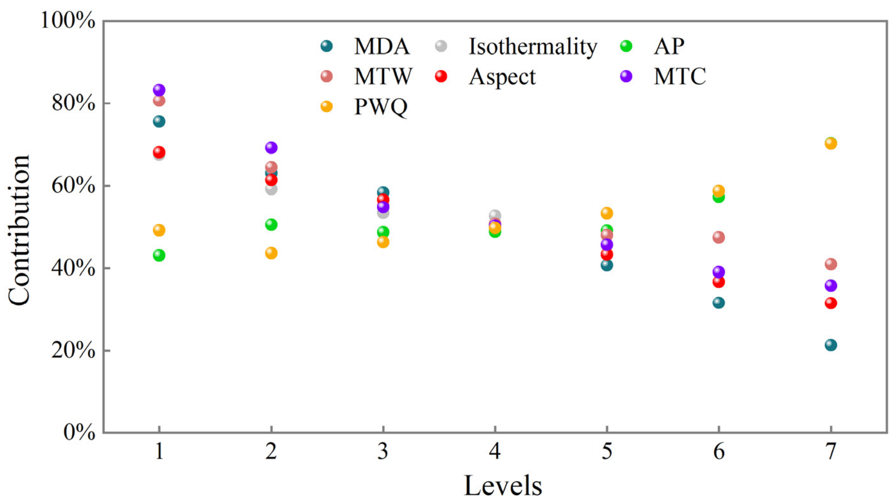

Figure 10. Internal hierarchical contribution diagram of different driving forces.

3.5. Watershed Vegetation Habitat Assessment

The preliminary analysis indicates that Aspect plays an important role in spatial heterogeneity of vegetation, so Aspect is selected as the explanatory variable, six bioclimatic variables as control variables, and the level of the explanatory variable (obtained by the Natural Breakpoint method) as the measurement index. The CSHRR model of the DTL basin was obtained. The CSHRR model constant β_0 of this basin is 2.56, and other parameters are shown in Table 3.

Table 3. CSHRR model parameters of Dongting Lake Basin.

Variable	Correlation Coefficient Value	Measure Index	Correlation Coefficient Value
Aspect	−0.035	T1	0.278
MDA	−1.685	T2	0.256
AP	0.596	T3	0.209
MTC	−0.433	T4	0.159
Isothermality	−0.746	T5	0.100
MTW	0	T6	0.044
PWQ	0.095	T7	0

Note: T is the coefficient of level value.

The whole basin vegetation habitat values were calculated by the CSHRR model and fitted with the MaxEnt model results (Figure 11). Pearson correlation coefficient achieved 0.854, and the residuals were shown in the upper left corner, where the residuals were mainly the point of concentrated (−0.15, 0.15). The above results show that the fitting effect is good. Spatially, the Empirical Bayesian Kriging Interpolation was used to display the results in the watershed space. The CSHRR model can describe the habitat status of indicator species in the basin well on the whole and can quantitatively give the vegetation habitat value of any region in the watershed (Figure 12).

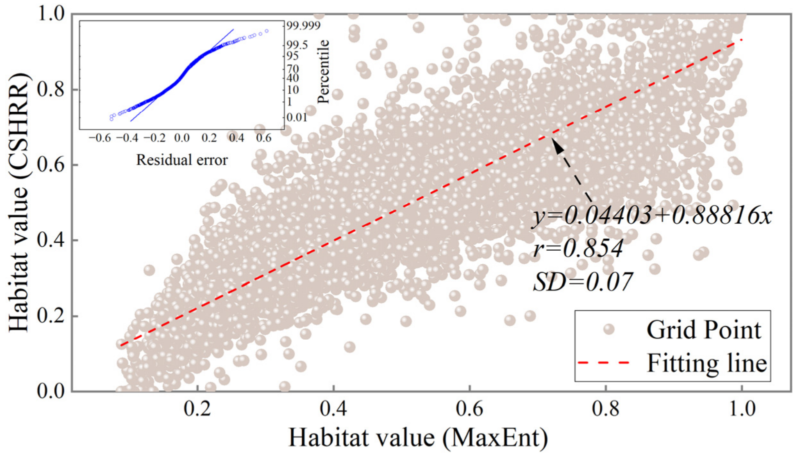

Figure 11. Vegetation habitat fitting in Dongting Lake basin.

The reliability of the CSHRR model is further verified by future climate data. The SSP2-4.5 path scenario refers to the decline of carbon dioxide emissions in the middle of this century, which is a moderate radiative forcing scenario, which is more in line with the current global climate environment [53]. The habitat status of the indicator species in 2021–2040 was simulated by the CSHRR model, and the results are shown in Figure 13. Compared with the results obtained by the MaxEnt model under future climate scenarios, the CSHRR model still maintains a high accuracy in the distribution of indicator species in watershed space. Under the radiative forcing scenario, the vegetation habitat conditions tend to deteriorate, and the habitat conditions remain at a moderate level, especially in the east and west, which are basically no longer suitable for the survival of the indicator species.

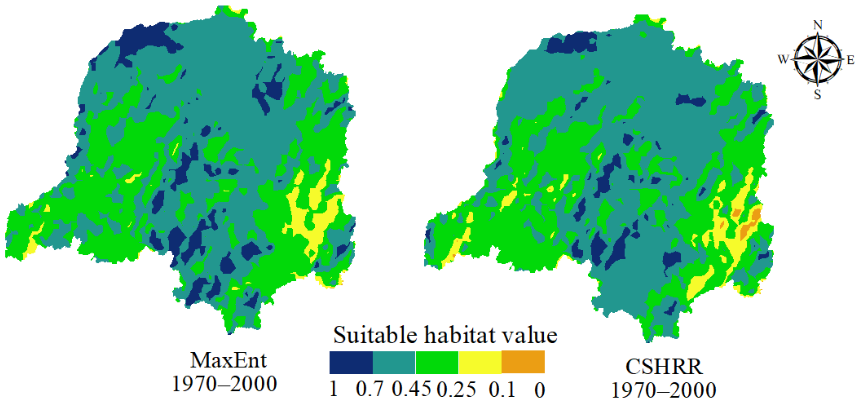

Figure 12. Vegetation habitat reconstruction under current climate (1970–2000). **Note:** Habitat quality values into 5 classes, including excellent (0.7–1), good (0.45–0.7), average (0.25–0.45), poor (0.1–0.25), and unsuitable habitats (0–0.1).

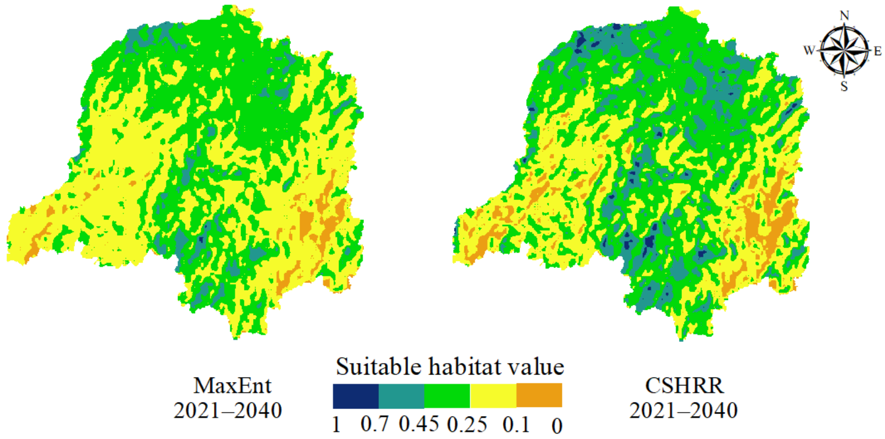

Figure 13. Reliability verification of CSHRR model.

4. Discussion

4.1. Model Evaluation and its Advantages

The mean AUC of the potential distribution of *Cryptomeria fortunei* in the DTL watershed, constructed by our MaxEnt model, was 0.832 with a standard error of 0.036. This result was greater than 0.7, indicating that the model's output was reasonable. However, the performance of the MaxEnt model was influenced by many hyperparameters, such as regularization strength, iteration number, and regularization multiplier [45]. In the next step, optimizing the parameters of the MaxEnt model can enhance the applicability of quantifying the response relationship between different factors and species. The correlation coefficients of our CSHRR model revealed an interesting result. Due to space constraints, we discuss Aspect and MDA as examples (Figure 14). Despite Aspect having a higher contribution to the species distribution, it showed a negative correlation (Correlation coefficient value = −0.035), which corresponds to the response curve of the MaxEnt model. When the Aspect reached a certain degree, it was unfavorable for the suitability of the species' habitat, and the MDA response curve also conveyed the same phenomenon. Combining the correlation coefficients of the variables, we can have a more intuitive understanding that the current DTL Basin is relatively suitable for the survival of *Cryptomeria fortunei*, and the quantitative relationships between different environmental factors and species distribution are revealed.

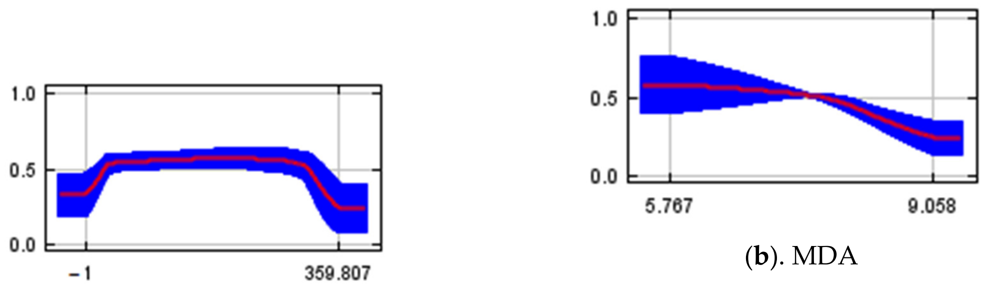

(**a**). Aspect (**b**). MDA

Figure 14. Factor response curve.

4.2. Attribution of Watershed Climate Change

In this study, we also described the relationship between AT, precipitation, and ETo in detail. AT, as an important physical factor driving water form transformation in the ecosystem, is also the basis for us to build the CSHRR model. Clarifying the correlation between AT and precipitation is helpful to further optimize and improve the model. The bioclimatic variables MDA, Isothermality, and MTW in the CSHRR model are all related to the maximum temperature. However, the maximum temperature sequence is not synchronized with the mean temperature and the minimum temperature in terms of abrupt change time (Figure 2). High-temperature events are mainly influenced by an increase in net shortwave radiation from the surface. The abnormal subsidence of the troposphere and the decrease in the water vapor content will promote the increase in the surface net shortwave radiation, leading to the occurrence of a high-temperature event [9]. This may be related to El Niño and the Southern Oscillation (ENSO) because there is generally a short cycle of about 2–8 years between them and precipitation [54,55]. In general, the La Nia phase of ENSO is accompanied by an increase in the frequency and intensity of excessive precipitation during one year and a decrease in both during the following year [56]. Among them, ENSO had an impact on the DTL basin in 1997 [57], which also explained why the sudden change point of the maximum temperature in the DTL basin lagged behind by one year. At the same time, we propose the De-interference Meteorological Analysis Technology to remove the interference of ETo and find that there is a significant negative correlation between precipitation and AT from 1963 to 1967 (Figure 5), a low positive correlation in 1997, and a low negative correlation in 2015. According to references [58,59], the DTL basin was affected by strong El Niño in 1953, and severe floods occurred in 1954, and then from 1963 to 1965, 1997, and 2015, heavy precipitation occurred under the influence of strong El Niño. This is because El Niño sometimes causes reverse circulation anomalies, resulting in an abnormally high regional high pressure [60], which generates the West Pacific subtropical high pressure in the DTL basin of the Yangtze River, thus forming a high-temperature climate. As a result, we think that El Niño is likely to have an impact on the negative partial correlation between AT and precipitation.

4.3. Improvement of CSHRR Model

It is worth noting that the CSHRR model does not have fixed variables. It is coupled with the MaxEnt model. The control and explanatory variables may vary for different species because each species has different environmental requirements [61]. The development of the CSHRR model aims to further enhance the practical value of the MaxEnt model in predicting animal and plant distributions [62,63].

In this study, Aspect is a key channel connecting water transport in the atmosphere and lithosphere, and Aspect is used as an explanatory variable in the CSHRR model. Above ground, Aspect involves vegetation canopy interception and evapotranspiration, such as vegetation sunshine duration and photosynthesis and other factors [64,65]. For below the surface, after precipitation, Aspect affects vegetation's access to water by controlling groundwater content, so groundwater flow is significantly affected by the Aspect [66]. As a result, the relationship between vegetation and Aspect can be seen as extending the impact of vegetation on changes in rainfall-ETo. We are also very concerned about how future climate scenarios will affect the suitability of vegetation for habitat. We further discuss the difference between current bioclimatic variables and future bioclimatic variables (Figure 15). MDA is the climate driving force with the highest contribution rate except for Aspect, and the difference shows that the boundary between the minimum temperature and the maximum temperature gradually shrinks (the difference fluctuates between −0.2 °C and 4 °C in most regions). The changes in Isothermality, MTW, and MTC all proved this trend, in which MTW increased by 2 °C and MTC increased by at least 1.5 °C. For vegetation in the northern hemisphere, when the temperature exceeds a certain threshold, their growth will be inhibited [4]. In terms of precipitation, the lower sections of the DTL basin and its surroundings will experience an increase in precipitation under the future climatic scenario, especially PWQ in the central part will decrease significantly. The occurrence of climate change is unstoppable, but human beings, as important participants and contributors to the ecosystem, cannot be ignored. More attention should be paid to studying the impact of future climate change on species distribution [30]. However, the impact of human activities on climate has been considered in future climate scenarios. However, for the response study of the future vegetation phenology model, we think that the next step can be to incorporate the positive elements of human activities (such as quantifying the policies of regional decision-makers on vegetation protection and the number of funds invested in related ecological restoration), so as to revise the response results of the CSHRR model to future scenarios.

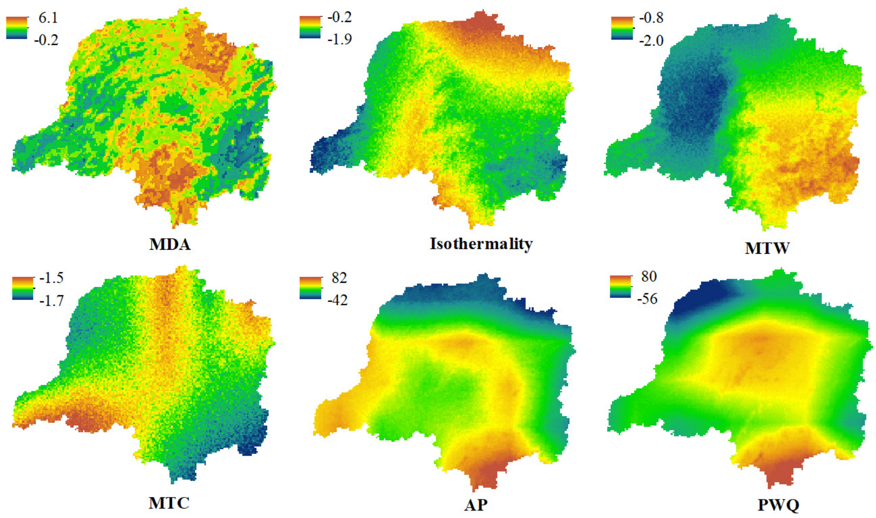

Figure 15. Difference between current bioclimatic variables and future bioclimatic variables in Dongting Lake Basin. **Note:** The difference is the raster value of current bioclimatic variables minus the raster value of future bioclimatic variables.

5. Conclusions

We examined the mode properties of AT, precipitation, and ETo and proposed the De-interference Meteorological Analysis Technology in light of the complexity of climate change and its ecological influence on vegetation. In order to quantify the relationship between climate and vegetation habitats, MLS-TLS was introduced, and CSHRR models were created by accounting for the influence of ecological factors. We found that the existence of evapotranspiration will make the AT-precipitation show a false negative correlation. We also obtained the degree of change in an extreme climate, in which the two indicators of temperature (TN90p, TX90p) have reached moderate changes, respectively 44% and 36%, while the extreme precipitation indicators are all low-level changes. We determined that Aspect and MDA were the primary influences on vegetation suitability and that MTC contributed 26% more to spatial heterogeneity than AP. The CSHRR model created using MLS-TLS has a good quantitative indicator function, which has practical value for assessing the potential distribution of local vegetation. This is in contrast to the qualitative analysis of the MaxEnt model. Its benefit is that depending on the quantitatively determining the influence coefficients of different driving forces, it can offer the most direct reference for the preservation of local vegetation or the repair of its ecological environment. In conclusion, the CSHRR model that we have proposed tries to provide some suggestions and aid in quantifying the impact of climate change. However, additional research into the model's positive benefits of human activity may produce more precise and realistic results.

Author Contributions: Conceptualization, W.G. and L.H.; methodology, P.Z.; software, L.H.; validation, L.H., N.H., and H.W.; formal analysis, M.L.; investigation, W.G.; resources, X.J.; data curation, L.H. and F.H.; writing—original draft preparation, L.H.; writing—review and editing, L.H.; visualization, M.L.; supervision, Y.N.; funding acquisition, Y.N. and W.G. All authors have read and agreed to the published version of the manuscript.

Funding: This work was supported by the National Key Research and Development Program of China (2022YFC3200017); the Basic Research Project of Key Scientific Research Projects of Colleges and Universities of Henan Province (23ZX012).

Data Availability Statement: Not applicable.

Acknowledgments: We would like to express our sincere gratitude to the editors and reviewers who have put considerable time and effort into their comments on this paper.

Conflicts of Interest: The authors have no conflicts of interest to declare.

References

1. Miguez-Macho, G.; Fan, Y. Spatiotemporal origin of soil water taken up by vegetation. *Nature* **2021**, *598*, 624. [CrossRef] [PubMed]
2. Anderegg, W.; Trugman, A.; Badgley, G.; Anderson, C.; Bartuska, A.; Ciais, P.; Cullenward, D.; Field, B.; Freeman, J.; Goetz, S.; et al. Climate-driven risks to the climate mitigation potential of forests. *Science* **2020**, *368*, 1327. [CrossRef] [PubMed]
3. Li, J.; Bevacqua, E.; Chen, C.; Wang, Z.; Chen, X.; Myneni, R.; Wu, X.; Xu, C.; Zhang, Z.; Zscheischler, J. Regional asymmetry in the response of global vegetation growth to springtime compound climate events. *Commun. Earth Environ.* **2022**, *3*, 123. [CrossRef]
4. Wu, X.; Guo, W.; Liu, H.; Li, X.; Peng, C.; Allen, C.; Zhang, C.; Wang, P.; Pei, T.; Ma, T.; et al. Exposures to temperature beyond threshold disproportionately reduce vegetation growth in the northern hemisphere. *Natl. Sci. Rev.* **2018**, *6*, 786–795. [CrossRef]
5. Zhang, M.; Lin, H.; Long, X.; Cai, Y. Analyzing the spatiotemporal pattern and driving factors of wetland vegetation changes using 2000-2019 time-series Landsat data. *Sci. Total Environ.* **2021**, *780*, 146615. [CrossRef]
6. Zhang, X.; Wu, S.; Yan, X.; Chen, Z. A global classification of vegetation based on NDVI, rainfall and temperature. *Int. J. Climatol.* **2017**, *37*, 2318–2324. [CrossRef]
7. Keenan, T.; Hollinger, D.; Bohrer, G.; Dragoni, D.; Munger, J.; Schmid, H.; Richardson, H. Increase in forest water-use efficiency as atmospheric carbon dioxide concentrations rise. *Nature* **2013**, *499*, 324–327. [CrossRef]
8. Mottl, O.; Flantua, S.; Bhatta, K.P.; Felde, V.; Giesecke, T.; Goring, S.; Grimm, E.; Haberle, S.; Hooghiemstra, H.; Ivory, S.; et al. Global acceleration in rates of vegetation change over the past 18,000 years. *Science* **2021**, *372*, 860–864. [CrossRef]
9. Zhu, B.; Sun, B.; Li, H.; Wang, H. Interdecadal Variations in Extreme High–Temperature Events over Southern China in the Early 2000s and the Influence of the Pacific Decadal Oscillation. *Atmosphere* **2020**, *11*, 829. [CrossRef]
10. Lynn, J.; Klanderud, K.; Telford, R.; Glodberg, D.; Vandvik, V. Macroecological context predicts species' responses to climate warming. *Glob. Change Biol.* **2021**, *27*, 2088–2101. [CrossRef]
11. Qiu, C.; Shen, Z.; Peng, P.; Mao, L.; Zhang, X. How does contemporary climate versus climate change velocity affect endemic plant species richness in China? *Chin. Sci. Bull.* **2014**, *59*, 4660–4667. [CrossRef]
12. Su, Y.; Guo, Q.; Guan, H.; Hu, T.; Jin, S.; Wang, Z.; Liu, L.; Jiang, L.; Guo, K.; Xie, Z.; et al. Human-Climate Coupled Changes in Vegetation Community Complexity of China Since 1980s. *Earth's Future* **2022**, *10*, e2021EF002553. [CrossRef]
13. Du, Q.; Sun, Y.; Guan, Q.; Pan, N.; Wang, Q.; Ma, Y.; Li, H.; Liang, L. Vulnerability of grassland ecosystems to climate change in the Qilian Mountains, northwest China. *J. Hydrol.* **2022**, *612*, 128305. [CrossRef]
14. Qiao, K.; Zhu, W.; Xie, Z. Application conditions and impact factors for various vegetation indices in constructing the LAI seasonal trajectory over different vegetation types. *Ecol. Indic.* **2020**, *112*, 106153. [CrossRef]
15. Yettella, V.; Weiss, J.; Kay, J.; Pendergrass, A. ensemble covariance framework for quantifying forced climate variability and its time of emergence. *J. Clim.* **2018**, *31*, 4117–4133. [CrossRef]
16. Qin, Y.; Li, B.; Chen, Z.; Chen, Y.; Lian, L. Spatio-temporal variations of nonlinear trends of precipitation over an arid region of northwest China according to the extreme-point symmetric mode decomposition method. *Int. J. Climatol.* **2017**, *38*, 2239–2249. [CrossRef]

17. Elith, J.; Phillips, S.; Hastie, T.; Dudík, M.; Chee, Y.; Yates, C. A statistical explanation of MaxEnt for ecologists. *Divers. Distrib.* **2011**, *17*, 43–57. [CrossRef]
18. Feng, H.; Bao, Q.; Ochoa, C.G. Long-term river water temperature reconstruction and investigation: A case study of the Dongting Lake Basin, China. *J. Hydrol.* **2023**, *616*, 128857.
19. Ma, B.; Zeng, W.; Xie, Y.; Wang, Z.; Hu, G.; Li, Q.; Cao, R.; Zhuo, Y. Boundary delineation and grading functional zoning of Sanjiangyuan National Park based on biodiversity importance evaluations. *Sci. Total Environ.* **2022**, *825*, 154068. [CrossRef]
20. Qin, Y.; Wang, C.; Zhao, Z.; Pan, X.; Li, Z. Climate change impacts on the global potential geographical distribution of the agricultural invasive pest, *Bactrocera dorsalis* (Hendel) (Diptera: Tephritidae). *Clim. Change* **2019**, *155*, 145–156. [CrossRef]
21. Merow, C.; Smith, M.J.; Silander, J.A. A practical guide to MaxEnt for modeling species' distributions: What it does, and why inputs and settings matter. *Ecography* **2013**, *36*, 1058–1069. [CrossRef]
22. Higgins, S.; Larcombe, M.; Beeton, N.; Conradi, T.; Nottebrock, H. Predictive ability of a process-based versus a correlative species distribution model. *Ecol. Evol.* **2020**, *10*, 11043–11054. [CrossRef] [PubMed]
23. Zheng, B.; Yang, Z. Perturbation analysis for mixed least squares–total least squares problems. *Numer. Linear Algebra Appl.* **2019**, *26*, e2239. [CrossRef]
24. Zhu, Y.; Wang, H.; Guo, W. The impacts of water level fluctuations of East Dongting Lake on habitat suitability of migratory birds. *Ecol. Indic.* **2021**, *132*, 108277. [CrossRef]
25. Li, Y.; Li, X.; Zhang, C.; Wang, X. Change Trend of Salix Ligneous Plants in the Dongting Lake Wetlands and Its Reasons. *Wetl. Sci.* **2014**, *12*, 646–649.
26. Dou, R.; Jiang, H.; Yu, S.; Ma, Y.; Guo, P. Decomposition of Cryptomeria fortunei leaf litter in subtropical and tropical China. *Acta Ecol. Sin.* **2010**, *30*, 1758–1763.
27. Xia, A.; Da, L.; Zhu, H.; Zhao, M. Community structure and regeneration pattern of Cryptomeria fortunei in Mount Tianmu of Zhejiang, China. *J. Zhejiang A F Univ.* **2004**, *21*, 46–52.
28. Zhang, J.; Xiao, H.; Fang, H. Component-based Reconstruction Prediction of Runoff at Multi-time Scales in the Source Area of the Yellow River Based on the ARMA Model. *Water Resour. Manag.* **2022**, *36*, 433–448. [CrossRef]
29. Zhou, T.; Zou, L.; Chen, X. Commentary on the Coupled Model Intercomparison Project Phase 6 (CMIP6). *Clim. Chang. Res.* **2019**, *15*, 445–456.
30. Zhao, Y.; Xiao, D.; Bai, H.; Tang, J.; Liu, D. Future Projection for Climate Suitability of Summer Maize in the North China Plain. *Agriculture* **2022**, *12*, 348. [CrossRef]
31. Suarez-Seoane, S.; Jimenez-Alfaro, B.; Obeso, J. Habitat-partitioning improves regional distribution models in multi-habitat species: A case study with the European bilberry. *Biodivers. Conserv.* **2020**, *29*, 987–1008. [CrossRef]
32. Zhao, G.; Tian, P.; Mu, X.; Jiao, J.; Wang, F.; Gao, P. Quantifying the impact of climate variability and human activities on streamflow in the middle reaches of the Yellow River basin, China. *J. Hydrol.* **2014**, *519*, 387–398. [CrossRef]
33. Wang, J.; Sun, X.; Cheng, Q.; Cui, Q. An innovative random forest-based nonlinear ensemble paradigm of improved feature extraction and deep learning for carbon price forecasting. *Sci. Total Environ.* **2021**, *762*, 143099. [CrossRef] [PubMed]
34. Wen, X.; Feng, Q.; Deo, R.; Wu, M.; Yin, Z.; Yang, L.; Singh, V. Two-phase extreme learning machines integrated with the complete ensemble empirical mode decomposition with adaptive noise algorithm for multi-scale runoff prediction problems. *J. Hydrol.* **2019**, *570*, 167–184. [CrossRef]
35. Meng, E.; Huang, S.; Huang, Q.; Fang, W.; Wu, L.; Wang, L. A robust method for non-stationary streamflow prediction based on improved EMD-SVM model. *J. Hydrol.* **2019**, *568*, 462–478. [CrossRef]
36. Chen, T.; Xie, Y.; Liu, C.; Bai, Y.; Zhang, A.; Mao, L.; Fan, S. Trend Analysis of Relationship between Primary Productivity, Precipitation and Temperature in Inner Mongolia. *ISPRS Int. J. Geo-Inf.* **2018**, *7*, 214. [CrossRef]
37. Zhao, J.; Cao, Y.; Wang, X. The Physical Significance of the Synthetic Running Correlation Coefficient and Its Applications in Oceanic and Atmospheric Studies. *J. Ocean. Univ. China* **2018**, *17*, 451–460. [CrossRef]
38. Jiang, S.; Zhou, L.; Ren, L.; Wang, M.; Xu, C.; Yuan, F.; Liu, Y.; Yang, X.; Ding, Y. Development of a comprehensive framework for quantifying the impacts of climate change and human activities on river hydrological health variation. *J. Hydrol.* **2021**, *600*, 126566. [CrossRef]
39. Torrence, C.; Compo, G. A Practical Guide to Wavelet Analysis. *Bull. Am. Meteorol. Soc.* **1998**, *79*, 61–78. [CrossRef]
40. Guo, A.; Chang, J.; Wang, Y.; Li, Y. Variation characteristics of rainfall-runoff relationship and driving factors analysis in Jinghe river basin in nearly 50 years. *Trans. Chin. Soc. Agric. Eng.* **2015**, *31*, 165–171.
41. Varotsou, E.; Jochumsen, K.; Serra, N.; Kieke, D.; Schneider, L. Interannual transport variability of Upper Labrador Sea Water at Flemish Cap. *J. Geophys. Res. Ocean.* **2015**, *120*, 5074–5089. [CrossRef]
42. Wu, X.; Shen, C. A new methodology for local cross-correlation between two nonstationary time series. *Phys. A Stat. Mech. Its Appl.* **2019**, *528*, 121307. [CrossRef]
43. Wang, H.; Huang, L.; Guo, W.; Zhu, Y.; Yang, H.; Jiao, X.; Zhou, H. Evaluation of ecohydrological regime and its driving forces in the Dongting Lake, China. *J. Hydrol.-Reg. Stud.* **2022**, *41*, 101067.
44. Bowen, A.K.M.; Stevens, M.H.H. Temperature, topography, soil characteristics, and NDVI drive habitat preferences of a shade-tolerant invasive grass. *Ecol. Evol.* **2020**, *10*, 10785–10797. [CrossRef]

45. Khan, A.M.; Li, Q.; Saqib, Z.; Khan, N.; Habib, T.; Khalid, N.; Majeed, M.; Tariq, A. MaxEnt Modelling and Impact of Climate Change on Habitat Suitability Variations of Economically Important Chilgoza Pine (*Pinus gerardiana* Wall.) in South Asia. *Forests* **2022**, *13*, 715. [CrossRef]
46. Wang, J.; Li, X.; Christakos, G.; Liao, Y.; Zhang, T.; Gu, X.; Zheng, X. Geographical Detectors-Based Health Risk Assessment and its Application in the Neural Tube Defects Study of the Heshun Region, China. *Int. J. Geogr. Inf. Sci.* **2010**, *24*, 107–127. [CrossRef]
47. Zhu, L.; Meng, J.; Zhu, L. Applying Geodetector to disentangle the contributions of natural and anthropogenic factors to NDVI variations in the middle reaches of the Heihe River Basin. *Ecol. Indic.* **2020**, *117*, 106545. [CrossRef]
48. Wang, J.; Xu, C. Geodetector: Principle and prospective. *Acta Geogr. Sin.* **2017**, *72*, 116–134.
49. Chen, T.; Feng, Z.; Zhao, H.; Wu, K. Identification of ecosystem service bundles and driving factors in Beijing and its surrounding areas. *Sci. Total Environ.* **2020**, *711*, 134687. [CrossRef] [PubMed]
50. Gu, T.; Luo, Z.; Guo, T.; Luo, T. A New Reconstruction Method for Measurement Data With Multiple Outliers. *IEEE Trans. Instrum. Meas.* **2022**, *71*, 1–9. [CrossRef]
51. Liu, Q.; Wang, M. On the weighting method for mixed least squares-total least squares problems. *Numer. Linear Algebra Appl.* **2017**, *24*, e2094. [CrossRef]
52. Wasko, C.; Nathan, R. The local dependency of precipitation on historical changes in temperature. *Clim. Chang.* **2019**, *156*, 105–120. [CrossRef]
53. Simolo, C.; Corti, S. Quantifying the role of variability in future intensification of heat extremes. *Nat. Commun.* **2022**, *13*, 7930. [CrossRef] [PubMed]
54. Thomas, J.; Prasannakumar, V. Temporal analysis of rainfall (1871–2012) and drought characteristics over a tropical monsoon-dominated State (Kerala) of India. *J. Hydrol.* **2016**, *534*, 266–280. [CrossRef]
55. Timmermann, A.; An, S.; Kug, J.; Jin, F.; Cai, W.; Capotondi, A.; Cobb, K.; Lengaigne, M.; McPhaden, M.; Stuecker, M.; et al. El Niño–Southern Oscillation complexity. *Nature* **2018**, *559*, 535–545. [CrossRef] [PubMed]
56. Li, X.; Zhang, K.; Gu, P.; Feng, H.; Yin, Y.; Chen, W.; Cheng, B. Changes in precipitation extremes in the Yangtze River Basin during 1960-2019 and the association with global warming, ENSO, and local effects. *Sci. Total Environ.* **2020**, *760*, 144244. [CrossRef] [PubMed]
57. Guo, R.; Zhu, Y.; Liu, Y. A Comparison Study of Precipitation in the Poyang and the Dongting Lake Basins from 1960–2015. *Sci. Rep.* **2020**, *10*, 3381. [CrossRef]
58. Hu, G.; Ma, D. A Study on the Precipitation Features and Water Regime of Flood Disaster in Dongting Lake Region during Late Spring and Early Summer of 2016. *Territ. Nat. Resour. Study* **2017**, *169*, 20–26.
59. Duan, D.; Chen, Y.; Zhang, G. The Impact of El Nino and Atmosphere General Circulation on Flooding of Dongting Lake Region in 1998. *J. Hunan Agric. Univ.* **1999**, *25*, 220–224.
60. Driver, P.; Reason, C. Variability in the Botswana High and its relationships with rainfall and temperature characteristics over southern Africa. *Int. J. Climatol.* **2017**, *37*, 570–581. [CrossRef]
61. Chen, Y.; Wu, B.; Min, Z. Stand Diameter Distribution Modeling and Prediction Based on Maximum Entropy Principle. *Forests* **2019**, *10*, 859. [CrossRef]
62. Jing, W.; Qi, G.; Ma, J.; Yonglin, R.; Wang, R.; Simon, M. Predicting the potential geographic distribution of Bactrocera bryoniae and Bactrocera neohumeralis (Diptera: Tephritidae) in China using MaxEnt ecological niche modeling. *J. Integr. Agric.* **2020**, *19*, 2072–2082.
63. Xu, X.; Zhang, H.; Yue, J.; Xie, T.; Xu, Y.; Tian, Y. Predicting Shifts in the Suitable Climatic Distribution of Walnut (*Juglans regia* L.) in China: Maximum Entropy Model Paves the Way to Forest Management. *Forests* **2018**, *9*, 103. [CrossRef]
64. Junguo, H.; Guomo, Z.; Xiaojun, X. Using an improved back propagation neural network to study spatial distribution of sunshine illumination from sensor network data. *Ecol. Model.* **2013**, *266*, 86–96. [CrossRef]
65. Kumar, A.; Jhariya, M.; Yadav, D.; Banerjee, A. Vegetation dynamics in Bishrampur collieries of northern Chhattisgarh, India: Eco-restoration and management perspectives. *Environ. Monit. Assess.* **2017**, *189*, 371. [CrossRef] [PubMed]
66. Nana, Z.; Fuliang, Y.; Li, C.; Zhang, L.; Liu, J.; Mu, W.; Wang, H. Soil Moisture Dynamics and Effects on Runoff Generation at Small Hillslope Scale. *J. Hydrol. Eng.* **2015**, *20*, 05014024.